A Photometric Study of the Eclipsing Binary LO Ursae Majoris

Edward J. Michaels
Waffelow Creek Observatory, 10780 FM 1878, Nacogdoches, TX 75961; astroed@ejmj.net

Received October 15, 2021; revised November 23, 2021; accepted November 24, 2021

Abstract Multicolor photometric observations of the eclipsing binary LO UMa are presented. Photometric models were determined simultaneously from four sets of light curves using the Wilson-Devinney program. The results indicate LO UMa is a semidetached Algol type binary with a mass ratio of q = 0.62 and primary and secondary star spectral types of F9 and K8, respectively. Based on available times of minimum light, the O – C curves revealed a sinusoidal oscillation with a period of about 16.4 years and an amplitude of 0.0238 day. Two possible causes of the period variation were considered, changes in the quadrupole moment of the secondary star caused by magnetic activity (Applegate mechanism) and the light-time effect of a third body orbiting the binary. It was found that the most plausible explanation for the period oscillation is an unseen body, with a mass of no less than 1.55 $M_{\odot}$, orbiting the binary. A main sequence star of this mass would be the dominant light source in the system. However, spectra and observed color do not support a star of this mass, nor did the photometric solution find any indication of third light. A massive non-radiating third body suggests a possible neutron star candidate.

1. Introduction

The variability of LO UMa (GSC 03002-00454) was discovered from two images taken with the 25-cm astrograph at Indiana University's Goethe Link Observatory (Williams 2001). Using Harvard College Observatory patrol plates, combined with visual and CCD observations, it was evident this variable was an Algol-type eclipsing binary with a deep primary eclipse and an orbital period of 1.856 days (Baldwin *et al.* 2001). The ASAS-SN Variable Star Database gives a mean visual magnitude of 12.86 with a primary eclipse amplitude of 1.87 (Jayasinghe *et al.* 2019; Shappee *et al.* 2014). The LAMOST DR5 catalog gives an effective temperature of 6018 K (Luo *et al.* 2015). There are several minima times available (48), but no precision multiband photometric observations have been published for this system.

In this paper, a photometric study of LO UMa is presented. The photometric observations and data reduction methods are presented in section 2. A period analysis is presented in section 3. Analysis of the light curves using the Wilson-Devinney (WD) model is presented in section 4. Discussion of the results is presented in section 5 and conclusions are presented in section 6.

2. Photometric observations

Multicolor photometric observations were acquired with a 0.36-m Ritchey-Chrétien robotic telescope located at the Waffelow Creek Observatory, Nacogdoches, Texas (https://obs.ejmj.net). A SBIG-STXL camera with a cooled KAF-6303E CCD (−20° C, 9 µm pixels) was used for imaging. Each night, images were obtained in four passbands: Johnson V and Sloan g', r', and i'. The observation dates and number of images acquired are shown in the Table 1 observation log. The images were calibrated using bias, dark, and flat frames. MIRA software (Mirametrics 2015) was used for image calibration and the ensemble differential aperture photometry of the light images. The locations of the comparison and check stars are shown in Figure 1, and Table 2 gives their coordinates and standard magnitudes. The standard magnitudes were taken from the AAVSO Photometric All-Sky Survey database (APASS; Henden *et al.* 2015). The instrumental magnitudes were converted to standard magnitudes using the APASS comparison star magnitudes. The Heliocentric Julian Date (HJD) of each observation was converted to orbital phase (φ) using the following epoch and orbital period: T_0 = 2459292.6600 and

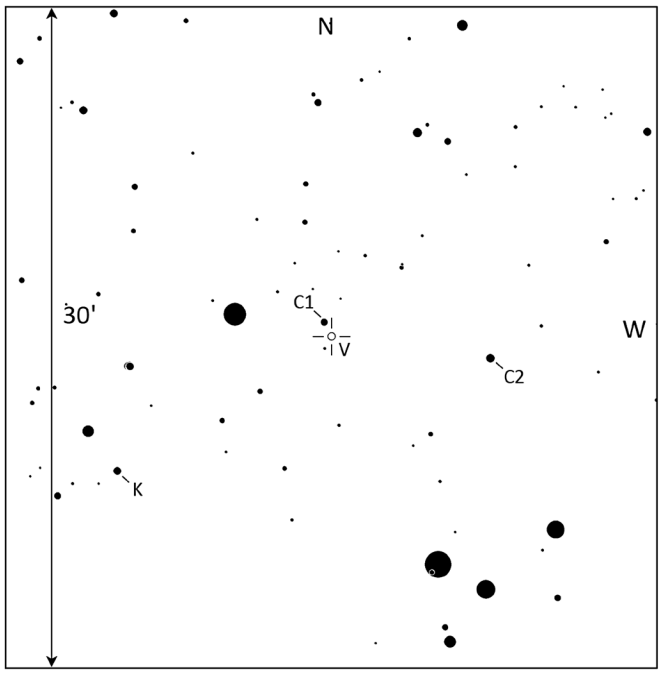

Figure 1. Finder chart for LO UMa (V), comparison stars (C1 and C2), and check (K) stars. This chart was generated by the AAVSO Variable Star Plotter (VSP; https://www.aavso.org/apps/vsp/).

Table 1. Observation log.

Filter	*Dates*	*No. Nights*	*No. Images*
V, g', r', i'	2021 Feb 22	1	66
V, g', r', i'	2021 Mar 18, 19, 23, 28, 31	5	280
V, g', r', i'	2021 Apr 1, 11, 18, 20, 21, 24	6	219
V, g', r', i'	2021 May 2, 4, 5, 6,13	5	181

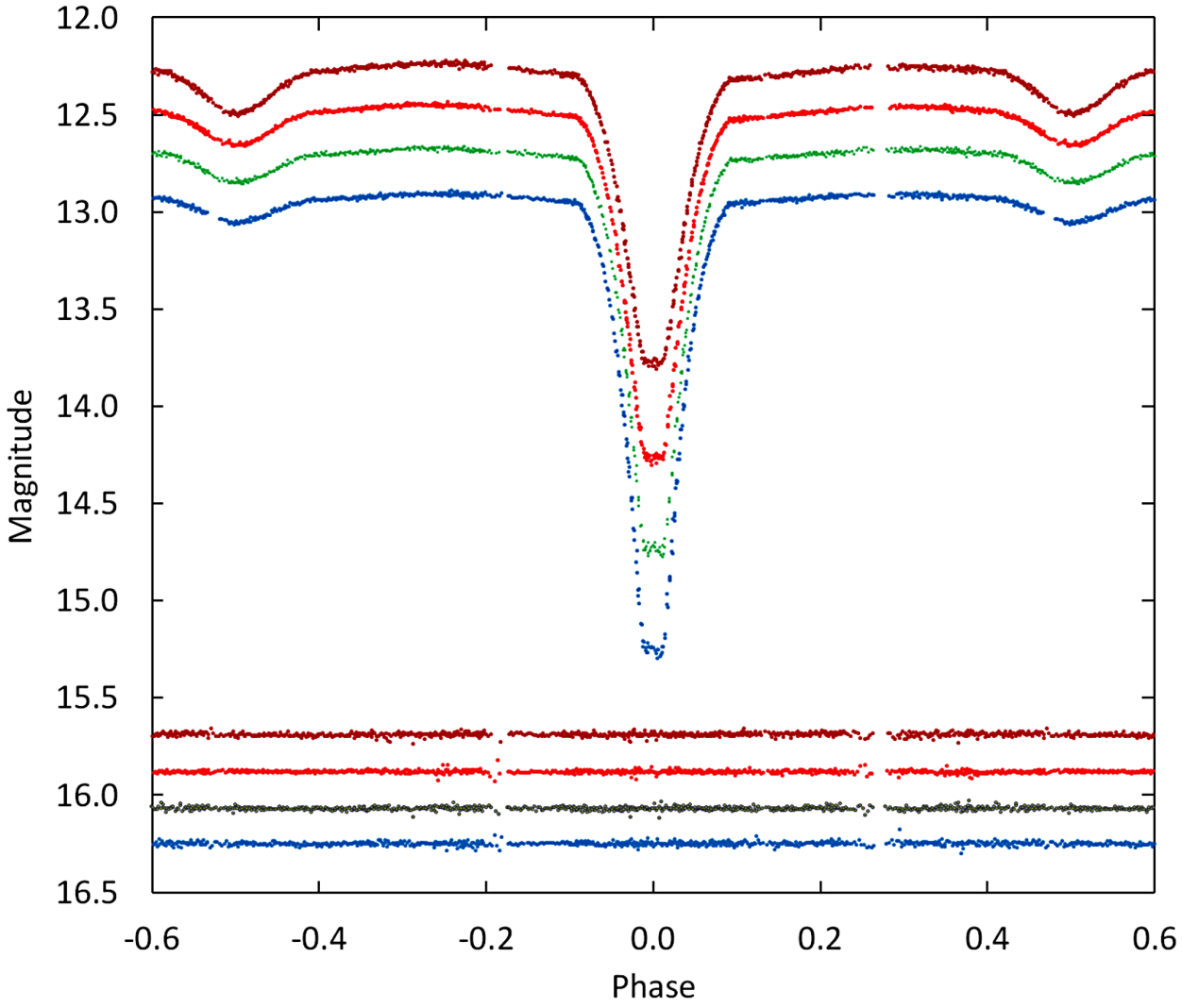

Figure 2. The folded CCD light curves in standard magnitudes. From top to bottom the passbands are i', r', V, and g'. In the same order, the bottom curves are the check-star magnitudes with offsets of +3.15, +3.15, +3.10, and +3.00 magnitudes, respectively. Error bars were omitted from the plotted points for clarity.

Table 2. APASS comparison and check star magnitudes.

System	*R.A. (2000)* *h*	*Dec (2000)* °	*V*	*g′*	*r′*	*i′*
LO UMa	10.497760	+ 39.94108				
GSC 03002-00277 (C1)	10.498258	+ 39.95172	13.227	13.365	13.105	12.999
GSC 03002-00389 (C2)	10.487341	+ 39.92442	12.810	13.149	12.501	12.240
GSC 03002-00145 (K)	10.511830	+ 39.83925	12.971	13.289	12.733	12.509
Standard deviation of K-star magnitudes			± 0.009	± 0.010	± 0.008	± 0.016

Table 3. Average light curve properties.

	Min I *Mag.*	*Min II* *Mag.*	*Δ Mag.* *Min II – Min I*	*Max I* *Mag.*	*Max II* *Mag.*	*Δ Mag.* *Max II – Max I*	*Mag. Range* *Max II – Min I*
V	14.731 ± 0.012	12.844 ± 0.003	–1.887 ± 0.012	12.675 ± 0.003	12.672 ± 0.003	–0.003 ± 0.004	2.059 ± 0.012
g'	15.255 ± 0.008	13.055 ± 0.006	–2.200 ± 0.010	12.910 ± 0.012	12.907 ± 0.004	–0.004 ± 0.013	2.348 ± 0.009
r'	14.264 ± 0.003	12.652 ± 0.002	–1.613 ± 0.003	12.464 ± 0.002	12.451 ± 0.001	–0.014 ± 0.003	1.814 ± 0.003
i'	13.775 ± 0.003	12.492 ± 0.002	–1.283 ± 0.003	12.253 ± 0.004	12.237 ± 0.002	–0.016 ± 0.005	1.539 ± 0.003

Note: Primary total eclipse duration: ~54 minutes.

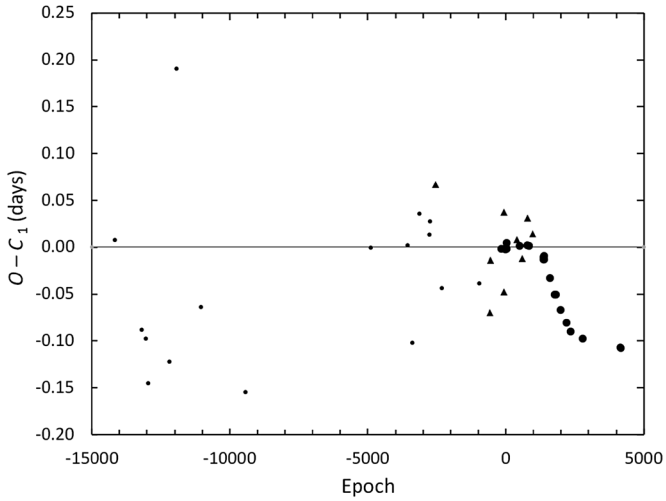

Figure 3. The residuals calculated from the linear ephemeris of Equation 1. The dots are the photovisual minima, the triangles the visual, and the filled circles the CCD.

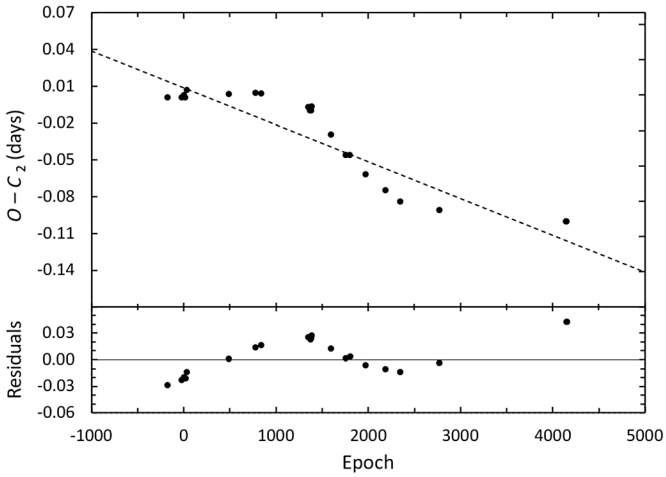

Figure 4. The top panel shows the residuals (filled circles) calculated from the linear ephemeris of Equation 1 using the CCD minima times from 1999–2021. The dashed line is the best–fit linear line from Equation 2. The bottom panel shows the residuals from the linear fit of Equation 2.

P = 1.8558690. Figure 2 shows the folded light curves plotted from orbital phase −0.6 to 0.6, with negative phase defined as (φ – 1). The nearly complete light curves required over two months of observations. The error of a single observation ranged from 7 to 23 mmag. The check star magnitudes were plotted and inspected each night, but no significant variability was found (see bottom of Figure 2). The standard deviations for all check star observations are listed in Table 2. The minimum light at primary eclipse for each passband was briefly constant, which confirms the total eclipse reported by Baldwin *et al.* (2001). The light curve properties for each passband are given in Table 3 (Min I, Min II, Max I, Max II, Δm, and total eclipse duration). The observations can be accessed from the AAVSO International Database (Kafka 2017).

3. Period study

A literature search located 42 minimum timings for this period study. From the current observations two new primary minima were found using the Kwee and van Woerden (1956) method. In addition, SuperWASP data were identified with sufficient cadence and light curve quality, from which another four minima were determined. All the minima times have been collected in Table 4. The difference between the observed and predicted eclipse timings, the $O - C_1$ residuals in Table 4, were calculated using Baldwin's (2001) linear ephemeris:

$$\text{HJD Min I} = 2451603.7691 + 1.8559010\ E. \quad (1)$$

These residuals are shown in Figure 3. Compared to the CCD minima, the photovisual and visual minima show a large amount of scatter (small dots and triangles in Figure 3). This is not unexpected given that each photovisual minima was determined from a single plate. These minima times occur at some point during the eclipse but not at mid-eclipse (Cycle Numbers: −14178 to −554, −63, −57). In addition, four of the visual minima covered only the ingress or the egress of a primary eclipse. The precision of the photovisual and most of the visual minima is unknown, since the standard errors were not provided.

A first attempt at a period analysis utilized only the CCD minima. Those observations are of higher accuracy and span 21 years (1999−2021). A least-squares solution to the residuals of Equation 1 gives the following new linear ephemeris:

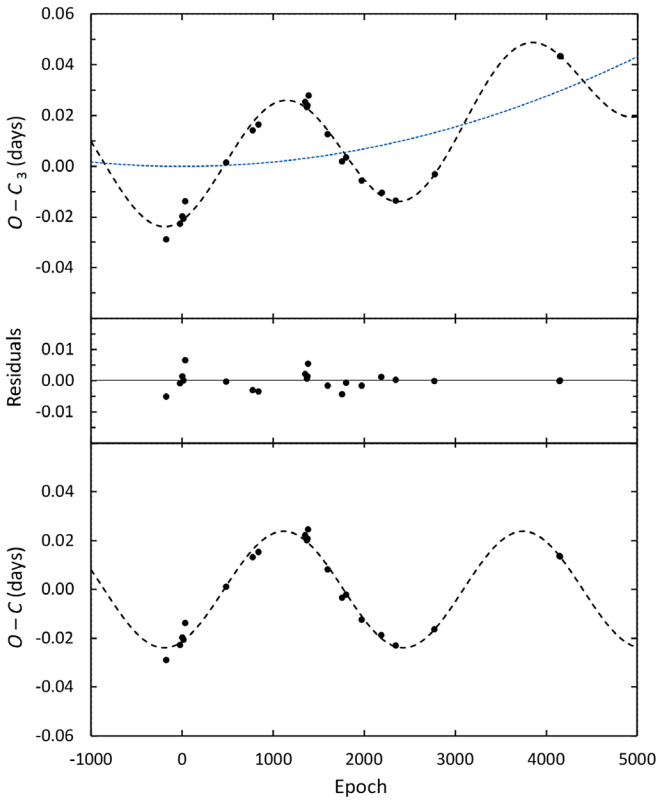

Figure 5. The Levenberg–Marquardt fit of the O−C residuals (filled circles) calculated from the updated linear ephemeris (Equation 2) using only the CCD minima times. In the top panel the dashed line shows the fit for a circular orbit (e = 0) for a supposed third body and the dotted (blue) line gives the quadratic fit from the residuals. The middle panel displays the total residuals after subtraction of both the upward parabolic change and the cyclic variation. The bottom panel shows the model fit after subtracting out the quadratic component.

$$\text{HJD Min I} = 2451603.7777\ (12) + 1.8558710\ (8)\ E. \quad (2)$$

This ephemeris should be useful in predicting the times of future primary eclipses. The results of the linear fit are displayed in the $O-C_2$ diagram of Figure 4 (top panel). The residuals plotted in the bottom panel provide information on any orbital period changes that may have occurred since 1999. Visual inspection of the residuals reveals possible sinusoidal and linear changes in the orbital period. A long-term linear change causes the O−C residuals to take on a parabolic shape, which is often attributed to mass transfer or angular momentum loss caused by magnetic braking. The cyclic variation may be the result of a third body orbiting the binary or magnetic activity of the stars. Each of these will be investigated in turn.

The motion of the binary around the barycenter of a tertiary system causes an apparent periodic change in the binary's orbital period. This results from the changing light travel time between Earth and the binary (Light-Time Effect or LITE). The period of the LITE oscillations corresponds to the orbital period of the binary and the tertiary component about their barycenter. An initial attempt to investigate both the parabolic and sinusoidal variations in the orbital period used the following equation:

$$\text{HJD Min I} = \text{HJD}_0 + \text{PE} + \text{QE}^2 + \text{A} \sin(\omega E + \varphi). \quad (3)$$

The computed result of the first three terms, $\text{HJD}_0 + \text{PE} + \text{QE}^2$, is the quadratic ephemeris where Q measures the long-term period change of the binary. The fourth term in Equation 3 is the time difference due to the binary's orbital motion about the barycenter. In this model, the periodic oscillation should appear symmetrical, and the orbit of the tertiary component is circular (e = 0). The parameter values HJD_0, P, Q, A, ω, and φ were determined using the Levenberg-Marquardt algorithm. The results (LITE-1) are displayed in Figure 5, and the calculated parameters are listed in column 2 of Table 5. The $O-C_3$ diagram in Figure 5 shows a possible long-term increase in the orbital period of the binary (dotted line). The calculated quadradic coefficient, $Q = 1.7\,(2) \times 10^{-9}$ d, measures this long-term change. The rate of period change since 1999 was calculated using the following equation:

$$\frac{dP}{dt} = \frac{2Q}{P} \cdot 365.24. \quad (4)$$

The orbital period appears to be increasing at a rate of $7\,(1) \times 10^{-7}$ d yr^{-1} or about 6 seconds per century. The coefficient of the sine term, A = 0.0238 ± 0.0002 d, is the semi-amplitude of the oscillation. The period of oscillation was calculated using the following equation:

$$P_3 = \frac{2\pi P}{\omega}, \quad (5)$$

where ω is the angular frequency and P the binary orbital period in days. The oscillation period, $P_3 = 13.36 \pm 0.09$ yr, is the orbital period of the binary and tertiary component about the barycenter. There are no additional periodic variations seen in the residuals (see center panel of Figure 5).

To analyze the possibility of a non-circular orbit, the sine term in Equation 3 was replaced with Irwin's (1959) formula:

$$\text{HJD (Min)}) = \text{HJD}_0 + \text{PE} + \text{QE}^2 + \frac{a_{12} \sin i_3}{c} \left[\frac{1 - e^2}{1 + e \cos \nu} \sin(\nu + \omega) + e \sin \omega \right]. \quad (6)$$

Table 4. Times of minima and O–C residuals.

Method	*Epoch HJD 2400000+*	*Error*	*Cycle No.*	*$(O-C)_1$*	*Ref.*
pg	25290.8130[a]	—	–14178.0	0.00828	1
pg	27092.7970	—	–13207.0	–0.08759	1
pg	27374.8840	—	–13055.0	–0.09755	1
pg	27532.5880	—	–12970.0	–0.14513	1
pg	28961.6550	—	–12200.0	–0.12190	1
pg	29429.6550[a]	—	–11948.0	0.19105	1
pg	31084.8640	—	–11056.0	–0.06364	1
pg	34072.7740[a]	—	–9446.0	–0.15425	1
pg	42485.7270	—	–4913.0	–0.00049	1
pg	44996.7640	—	–3560.0	0.00246	1
pg	45289.8920[a]	—	–3402.0	–0.10190	1
pg	45757.7170	—	–3150.0	0.03605	1
pg	46438.8100	—	–2783.0	0.01338	1
pg	46492.6460	—	–2754.0	0.02825	1
pg	46878.7120	—	–2546.0	0.06685	1
pg	47264.6290[a]	—	–2338.0	–0.04356	1
pg	49801.6510	—	–971.0	–0.03823	1
vis	50545.8360	—	–570.0	–0.06953	2
vis	50573.7300	—	–555.0	–0.01404	2
vis	50575.5860	—	–554.0	–0.01395	2
ccd	51273.4170	—	–178.0	–0.00172	3
vis	51486.8850	—	–63.0	0.03766	2
vis	51497.9350	—	–57.0	–0.04774	2
ccd	51551.8020	0.0030	–28.0	–0.00187	2
ccd	51603.7691	0.0001	0.0	0.00000	2
ccd	51629.7502	0.0002	14.0	–0.00151	2
ccd	51656.6670	0.0020	28.5	0.00472	2
vis	52368.4080	0.005	412.0	0.00769	4
ccd	52500.1707	—	483.0	0.00142	5
vis	52691.3150	—	586.0	–0.01209	6
ccd	53038.3828	0.0002	773.0	0.00223	7
vis	53049.5470	0.0090	779.0	0.03102	8
ccd	53157.1601	0.0010	837.0	0.00186	7
vis	53409.5750	0.0070	973.0	0.01423	9
ccd	54103.6577[b]	0.0001	1347.0	–0.01008	10
ccd	54142.6287[b]	0.0001	1368.0	–0.01299	10
ccd	54155.6204[b]	0.0001	1375.0	–0.01261	10
ccd	54170.4710[b]	0.0001	1383.0	–0.00921	10
ccd	54562.0423	—	1594.0	–0.03299	11
ccd	54860.8250	0.0008	1755.0	–0.05035	12
ccd	54942.4844	0.0004	1799.0	–0.05060	13
ccd	55259.8273	0.0010	1970.0	–0.06677	14
ccd	55660.6883	0.0003	2186.0	–0.08039	15
ccd	55953.9111	0.0005	2344.0	–0.08994	16
ccd	56038.7184[a]	0.0029	2389.5	0.27386	16
ccd	56744.5178	0.0003	2770.0	–0.09707	17
ccd	59292.6600	0.0003	4143.0	–0.10693	18
ccd	59305.6511	0.0002	4150.0	–0.10720	18

(a) CCD outlier not used in the period analysis. (b) Minima determined from SuperWASP data. References: (1) Williams (2001); (2) Baldwin et al. *(2001); (3) Paschke and Brat (2021); (4) Locher* et al. *(2002); (5) Kreiner (2004); (6) Diethelm (2003); (7) Krajci (2005); (8) Diethelm (2004); (9) Locher (2005); (10) Butters* et al. *(2010); (11) Nagai (2009); (12) Diethelm (2009); (13) Hübscher* et al. *(2010); (14) Diethelm (2010); (15) Diethelm (2011); (16) Diethelm (2012); (17) Hübscher (2015); (18) This paper.*

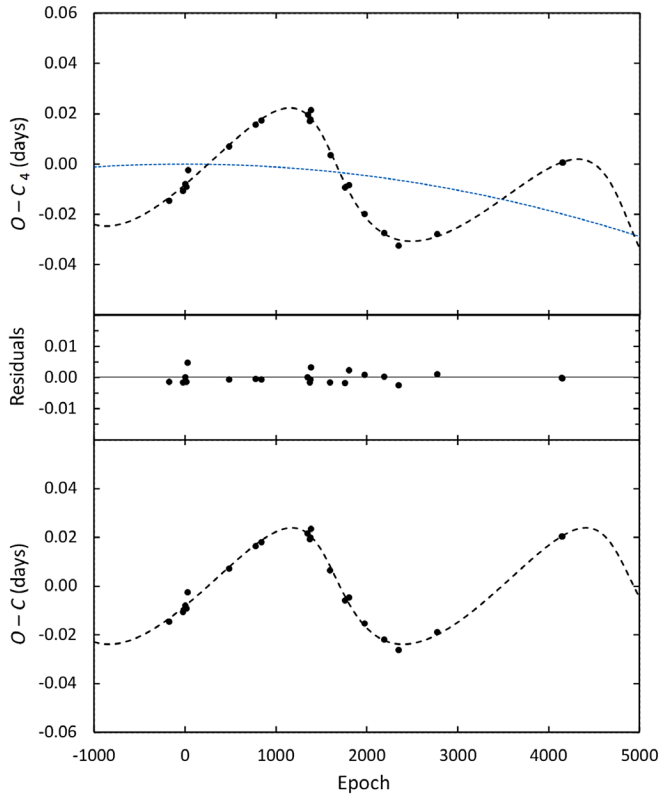

Figure 6. The simplex fit of the O – C residuals (filled circles) calculated from the updated linear ephemeris (Equation 2) using only CCD minima times. In the top panel the dashed line shows the fit for an elliptical orbit (e = 0.42) for a supposed third body and the dotted (blue) line defines the quadratic fit from the residuals. The middle panel displays the total residuals after subtraction of both the upward parabolic change and the cyclic variation. The bottom panel shows the model fit after subtracting out the quadratic component.

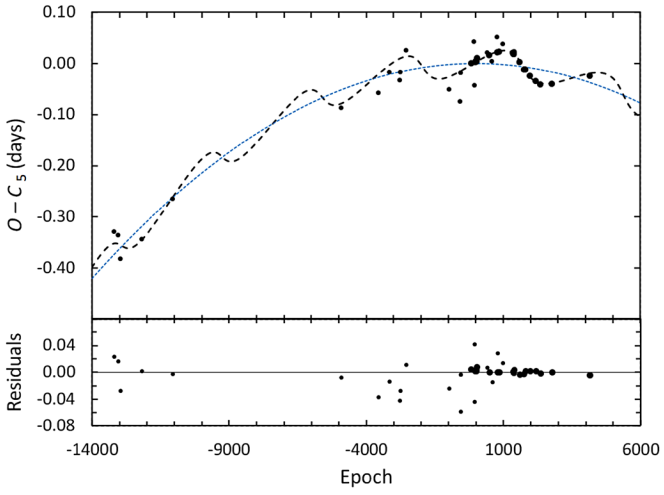

Figure 7. The simplex fit of the O – C residuals (dots) calculated from the Equation 1 linear ephemeris using all available minima times (CCD, photovisual, and visual). In the top panel the dashed line shows the fit for an elliptical orbit (e = 0.47) for a supposed third body and the dotted (blue) line defines the quadratic fit from the residuals. The bottom panel displays the total residuals remaining after LITE analysis.

Table 5. Parameters of the tertiary component.

Parameter	*CCD minima only* *LITE 1*	*LITE 2*	*All minima* *LITE 3*
JD_0 [HJD]	2451603.7887(5)	2451603.777(7)	2451603.763(5)
P [day]	1.8558600(8)	1.855873(4)	1.855882(2)
P_3 [yr]	13.36(9)	16.4(3)	18.6(3)
T_0 [HJD]	—	2454529(81)	2454771(403)
ω [°]	—	159(5)	177(19)
e	0	0.42(4)	0.47(33)
A_3 [day]	0.0238(2)	0.0238(8)	0.0273(5)
$a_{12} \sin i_3$ [a.u.]	4.4(1)	4.5(1)	5.4(9)
$f(M_3)$ [$M_\odot$]	0.39(1)	0.33(3)	0.45(7)
M_3 (i = 90°) [$M_\odot$]	1.68(3)	1.55(6)	1.8(2)
M_3 (i = 60°) [$M_\odot$]	2.09(4)	1.91(7)	2.2(2)
M_3 (i = 30°) [$M_\odot$]	5.5(9)	4.9(2)	6.0(7)
Q [day] [10^{-9}]	1.734(2)	–1.1518(8)	–2.1414(3)
dP/dt [10^{-7} d/y]	7(1)	–4.534(3)	–8.429(1)
Sum Res^2	0.00154	0.00063	—

Table 6. Results derived from light-curve modeling.

Parameter	*No Spots*	*Spots*
i (°)	85.96 ± 0.12	86.02 ± 0.09
T_1 (K)	6018[1]	6018[1]
T_2 (K)	3975 ± 9	3980 ± 4
Ω_1	4.963 ± 0.017	4.959 ± 0.013
Ω_2	3.107[2]	3.091[2]
q (M_2 / M_1)	0.624 ± 0.003	0.615 ± 0.002
$L_1 / (L_1 + L_2)$ (V)	0.8135 ± 0.0009	0.8130 ± 0.0006
$L_1 / (L_1 + L_2)$ (g')	0.8555 ± 0.0007	0.8550 ± 0.0007
$L_1 / (L_1 + L_2)$ (r')	0.7718 ± 0.0010	0.7714 ± 0.0006
$L_1 / (L_1 + L_2)$ (i')	0.7062 ± 0.0013	0.7060 ± 0.0009
r_1 side	0.2255 ± 0.0008	0.2280 ± 0.0007
r_2 side	0.3330 ± 0.0004	0.3304 ± 0.0003
Residuals	0.00070	0.00040
Star 1		*Hot Spot*
co-latitude (°)	—	85 ± 12
longitude (°)	—	24 ± 2
spot radius (°)	—	10 ± 5
temp. factor	—	1.06 ± 0.06
Star 1		*Cool Spot*
co-latitude (°)	—	120 ± 6
longitude (°)	—	288 ± 3
spot radius (°)	—	15 ± 9
temp. factor	—	0.92 ± 0.11
Star 2		*Hot Spot*
co-latitude (°)	—	76 ± 3
longitude (°)	—	13 ± 2
spot radius (°)	—	12 ± 4
temp. factor	—	1.16 ± 0.06

Note: The errors in the stellar parameters result from the least–squares fit to the model. The actual uncertainties are considerably larger. The subscripts 1 and 2 refer to the star being eclipsed at primary and secondary minimum, respectively. [1]*Assumed.* [2]*Calculated.*

Table 7. Provisional absolute parameters.

Parameter	*Symbol*	*Value*
Stellar masses	M_1 ($M_\odot$)	1.10 ± 0.11
	M_2 ($M_\odot$)	0.68 ± 0.07
Semi–major axis	a ($R_\odot$)	7.7 ± 0.2
Mean stellar radii	R_1 ($R_\odot$)	1.78 ± 0.08
	R_2 ($R_\odot$)	2.60 ± 0.09
Bolometric magnitude	$M_{bol,1}$	3.3 ± 0.1
	$M_{bol,2}$	4.3 ± 0.4
Stellar luminosity	L_1 ($L_\odot$)	3.7 ± 0.4
	L_2 ($L_\odot$)	1.5 ± 0.4
Surface gravity	log g_1 (cgs)	3.98 ± 0.05
	log g_2 (cgs)	3.44 ± 0.05

Note: The calculated values in this table are provisional. Radial velocity observations are necessary for direct determination of M_1, M_2, and a.

The tertiary component's associated orbital parameters for this term include the orbital period P_3, inclination i_3, orbital eccentricity e, amplitude $A = a_{12} \sin i_3$, argument of periastron ω, and time of periastron passage T_0. A simplex optimization was used to solve for the parameters using the MATLAB code written by Zasche *et al.* (2009). The initial parameter values were taken from the LITE-1 solution. The results (LITE-2) are listed in column 3 of Table 5 and are displayed in Figure 6. This solution gave a better fit, with a 41% reduction in residuals, compared to a circular orbit solution (LITE-1). To include information from the photovisual and visual minima times dating back to 1933, a third LITE solution (LITE-3) was attempted. This solution utilized most of the minima timings in Table 4 (photovisual, visual, and CCD), with only a few outliers excluded (Cycles −14178, −11948, −9446, −3402, and −2338). An arbitrary weighting scheme was applied, with w = 10 for CCD and w = 1 for photovisual and visual minima. The initial parameter values were taken from the LITE-2 solution. The results are tabulated in column 4 of Table 5 and displayed in Figure 7. The tertiary component masses listed in Table 5 were derived for each LITE solution using the mass function of the third body and the fitted parameters $A = a_{12} \sin i_3$ and P_3. The mass function is given by:

$$f(M_3) = \frac{(M_3 \sin i_3)^3}{(M_1 + M_2 + M_3)^2} = \frac{4\pi^2}{G P_3^2} (a_{12} \sin i_3)^3 , \quad (7)$$

where G is the gravitational constant, $M_1 = 1.10 \pm 0.11\, M_\odot$, and $M_2 = 0.68 \pm 0.07\, M_\odot$ (see section 5 for binary component masses). The minimum mass occurs when the orbit of the tertiary component is co-planar with the binary's orbit ($i_3 = 90°$). For each LITE solution, Table 5 lists the values for the mass function f(m), the semimajor axis of the binary's orbit about the barycenter ($a_{12} \sin i_3$), and the tertiary masses for inclinations of 30°, 60°, and 90°. The tertiary component's minimum mass ranged from $1.6\, M_\odot$ to $1.8\, M_\odot$ for the three LITE solutions. Main sequence stars in this mass range would have approximate luminosities of 7–9 $L_\odot$ and temperatures from 7200 K to 7600 K. The observed color and the LAMOST spectra do not support a star of this temperature in the system. A tertiary component of this luminosity would also greatly reduce the eclipse depths and would result in large third-light values (l_3) during Roche modeling. The results of the LITE solutions will be discussed further in section 5.

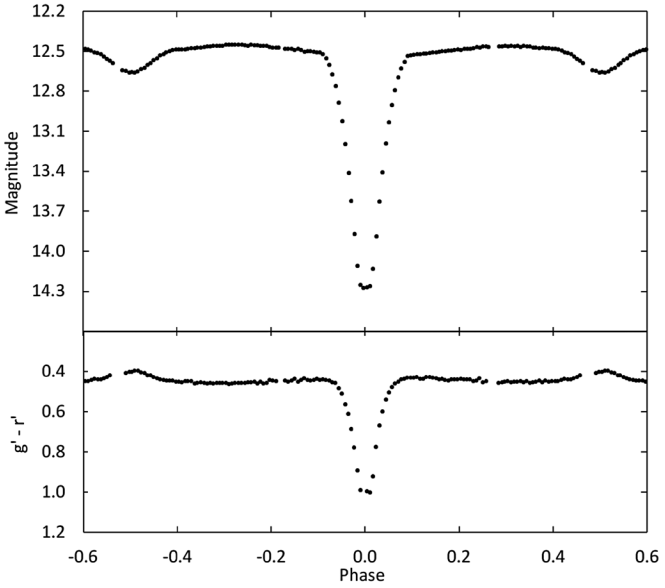

Figure 8. Light curve of the binned Sloan r' passband observations in standard magnitudes (top panel). The observations were binned with a phase width of 0.0067. The errors for each binned point are about the size of the plotted points. The (g' – r') colors (bottom panel) were calculated by subtracting the linearly interpolated binned g' and r' magnitudes.

Alternate explanations for a modulated orbital period include magnetic cycles in late-type stars and apsidal motion. Algol binaries with short orbital periods (<6 days) have circular orbits and are tidally locked, thus making apsidal motion unlikely as the cause of period modulation (Qian *et al.* 2018). The period changes may be caused by the Applegate mechanism, which postulates a change in the gravitational quadrupole moment of the binary's magnetically active secondary star (Applegate 1992; Lanza and Rodonò 1999; Völschow *et al.* 2016). This change is caused by the redistribution of angular momentum within the star due to the magnetic activity. To drive a period oscillation, a certain amount of energy is required to build a strong magnetic field. Eventually this field is dissipated, only to be built and dissipated again in a hydromagnetic dynamo cycle. A detailed investigation of the energetics ($\Delta E / E_{sec}$) was done by Völschow *et al.* (2016). The ratio $\Delta E / E_{sec}$ gives the energy necessary to drive the Applegate mechanism over the available energy produced by the magnetically active secondary star. This quantity determines the feasibility of the Applegate mechanism for LO UMa. The assessment of this mechanism for driving the period variations used Völschow *et al.*'s (2016) analytical two-zone model with different densities for the secondary's core and its convective shell. The $\Delta E / E_{sec}$ value was calculated using the "Eclipsing Time Variation Calculator" web module (http://theory-starformation-group.cl/applegate/index.php; Völschow *et al.* 2016). The module requires the following measured quantities for the calculation: the secondary star's mass (M_{sec}), radius (R_{sec}), and temperature (T_{sec}); the semimajor axis of the binary (a_{bin}); and $\Delta P / P_{bin}$, which is given by:

$$\frac{\Delta P}{P_{bin}} = 2\pi \frac{A_{o-c}}{P_{mod}} . \quad (8)$$

The calculations for this approximation used parameter values from each LITE solution and stellar parameters from Table 7 (see section 5). The resulting $\Delta E / E_{sec}$ values for LITE-1, LITE-2, and LITE-3 were 3.7, 1.9, and 1.7, respectively. In each case the relative threshold energy is greater than unity, indicating the energy necessary to drive the period oscillations is greater than the total energy generated by the secondary star. This implies the period modulation cannot be explained by the secondary star's magnetic activity. The period of modulation (P_{mod}) can also be estimated using the empirical relationship derived by Lanza and Rodonò (1999):

$$\log P_{mod} = -0.36\,(\pm 0.10) \log \Omega + 0.018, \quad (9)$$

where $\Omega = 2\pi / P$, P_{mod} is in years, and P is in seconds. Equation 9 predicts a modulation period of about 40 years, which is much longer than the values found in the LITE analysis (13.4–18.6 years). This result also indicates magnetic activity is unlikely the cause of the period modulation.

4. Light curve analysis

4.1. Color, temperature, spectral type, absolute magnitude, and luminosity

For measuring color change and Roche modeling, the large number of photometric observations was binned in both phase and magnitude. This resulted in 150 points for each color with a phase width of 0.0067. The phases and magnitudes of the observations in each bin were averaged. For color index, the binned r' magnitudes were then subtracted from the linearly interpolated g' magnitudes. The binned points of the r' light curve and the (g'−r') color index are shown in Figure 8. The large color change during primary eclipse indicates a significant temperature difference between the primary and secondary stars. The average observed color over the entire phase range is $(g'-r') = 0.479 \pm 0.010$. The color excess for this system, $E(g'-r') = 0.020 \pm 0.015$, was determined from dust maps based on Pan-STARRS1 and 2MASS photometry and Gaia parallaxes (Green *et al.* 2018). Subtracting the color excess from the average observed color gives an intrinsic color of $(g'-r')_o = 0.46 \pm 0.02$.

The LAMOST spectral survey DR5 catalog gives an effective temperature of $T_{eff} = 6018 \pm 34$ K for LO UMa's primary star (Luo *et al.* 2015). The LAMOST pipeline measures the spectra as single stars even though in the case of Algol binaries, there are two stars of different temperatures. There are subtle differences between the spectra of Algol binaries and single stars (Qian *et al.* 2018). This results in a small systematic bias of less than 200 K in the effective temperature. For stars with temperature differences larger than 1000 K, as is the case for LO UMa, the systematic biases are even smaller. The effective temperature's error was set to ± 100 K to account for this bias. The observed color index can also be used to estimate the effective temperature. The dereddened color at orbital phase $\varphi = 0.5$ is $(g'-r') = 0.379 \pm 0.016$. At this orbital phase, the secondary star's contribution to the total light is at a minimum. The effective temperature for this color, $T_{eff} = 6055 \pm 106$ K, was interpolated from Table 5 of Pecaut and Mamajek (2013). The effective temperatures from both methods are consistent, giving a spectral type of F9 for the primary star.

The absolute visual magnitude at quadrature ($\varphi = 0.75$), $M_v = 2.94 \pm 0.06$, was calculated using the Gaia distance and the apparent visual magnitude corrected for extinction. Using the bolometric correction for the effective temperature gives the combined luminosity of both stars, $L_{12} = 5.5 \pm 0.3\ L_{\odot}$ (Pecaut and Mamajek 2013).

4.2. Synthetic light curve modeling

Simultaneous four-color light curve solutions were obtained using the 2015 version of the Wilson-Devinney (WD) program (Wilson and Devinney 1971; van Hamme and Wilson 1998). The input data consisted of 150 normal points for each color (see section 4.1). The normal points were converted from magnitudes to flux, with each point assigned a weight equal to the number of observations forming that point.

The light curves (see Figure 2) display a deep primary minimum that is briefly total, a shallow secondary minimum, and small brightness changes outside of eclipses. This light curve morphology is typical of an Algol binary where there are large temperature differences between the component stars. Algols are binaries that are often detached with spherical or slightly elliptical components, but some are semidetached with one star filling its Roche lobe. Not knowing the configuration of this system, the WD program was initially configured to Mode-2 for detached binaries. The primary star's effective temperature was fixed at $T_1 = 6018$ K (see section 4.1). The subscripts 1 and 2 refer to the hotter and cooler components, respectively. With both component temperatures less than 7500 K, internal energy transfer to the surface is due to convection rather than radiative transfer. Standard convective parameters were used: gravity brightening, $g_1 = g_2 = 0.32$ (Lucy 1968) and bolometric albedo, $A_1 = A_2 = 0.5$ (Ruciński 1969). Logarithmic limb-darkening coefficients were calculated by the program from tabulated values using the method of van Hamme (1993). The adjustable parameters include the inclination (i), mass ratio ($q = M_2 / M_1$), potentials (Ω_1, Ω_2), temperature of the secondary star (T_2), band-specific luminosity for each wavelength (L), and third light (l). Given the evidence for a possible tertiary component (see section 3), third light was included from the beginning and throughout the solution process.

Preliminary fits to each light curve were made using the BINARY MAKER 3.0 program (BM3; Bradstreet and Steelman 2002). The primary star's temperature was set to 6018 K, standard convective parameters were used, and limb-darkening coefficients were taken from van Hamme's (1993) tabular values. The other parameters—inclination, mass ratio, potentials, and secondary star temperature—were adjusted in sequence until a good fit was obtained between the synthetic light curves and the observations for each passband. The parameters from the BM3 synthetic light curve fits were then averaged and used as the inputs for the computation of simultaneous four-color light curve solutions with the WD program. The Mode-2 iterations quickly converged to a semidetached configuration. Subsequent runs and solutions used Mode-5, in which the secondary potential (Ω_2) was no longer adjustable. A preliminary WD solution was completed using the Kurucz (2002) stellar atmosphere radiation

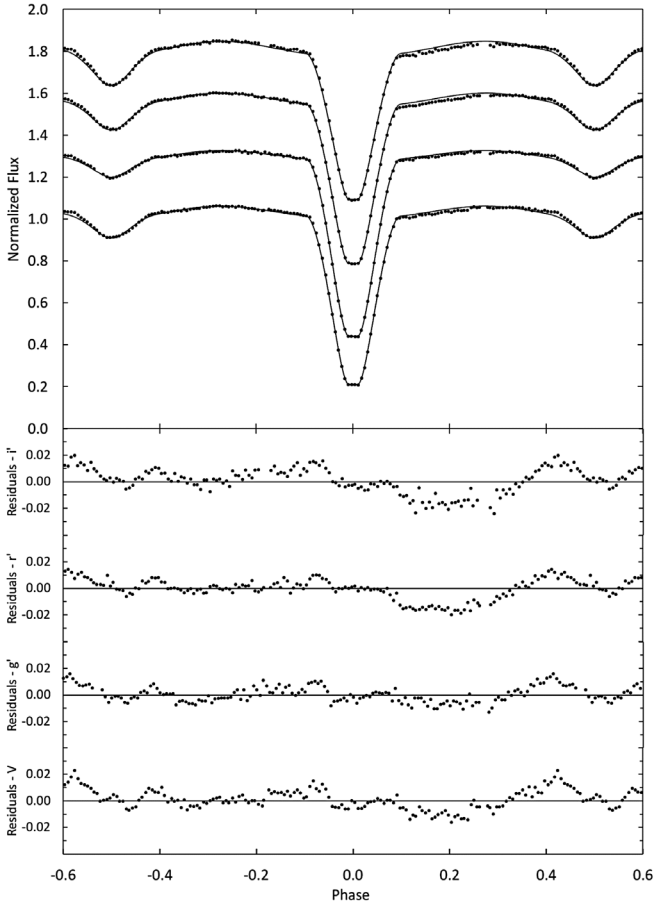

Figure 9. Comparison between the WD spotless best-fit model (solid curve) and the observed normalized flux curve. From top to bottom, the passbands are i', r', g', and V. Each light curve is offset by 0.25 for this combined plot. The residuals are shown in the bottom panel. Error bars are omitted from the points for clarity.

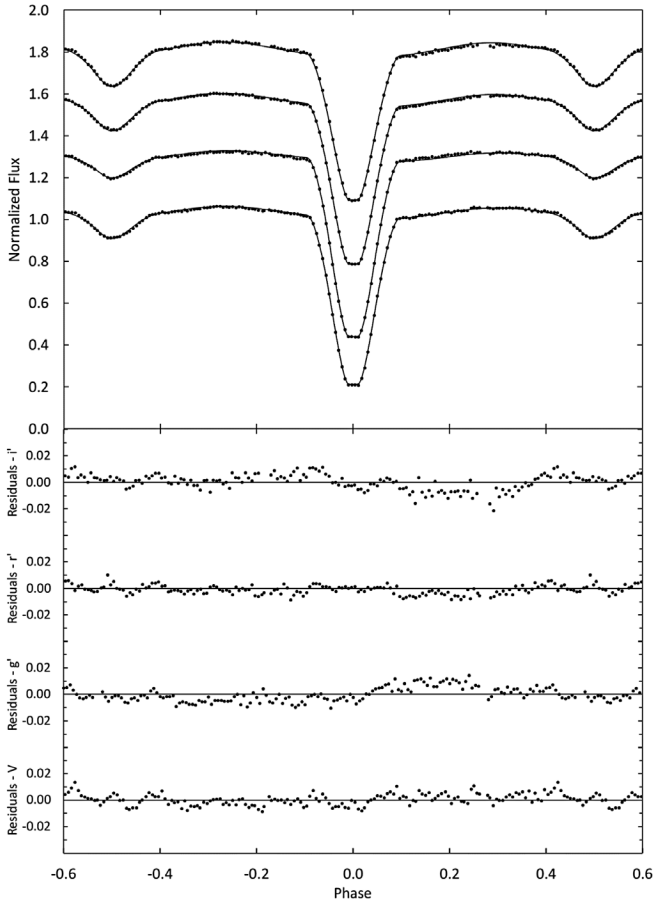

Figure 10. Comparison between the WD spotted best-fit model (solid curve) and the observed normalized flux curve. From top to bottom, the passbands are i', r', g', and V. Each light curve is offset by 0.25 for this combined plot. The residuals are shown in the bottom panel. Error bars are omitted from the points for clarity.

formulas, but this solution resulted in poor fits to the g'- and V-band observations. The final solution iterations were performed using blackbody radiation formulas, which resulted in better fits in all four passbands. The best-fit final solution parameters are shown in column 2 of Table 6. Figure 9 displays the normalized light curves overlaid by the synthetic solution curves (solid line), with the residuals in the bottom panel. Spectroscopic observations are not available to verify the mass ratio (q) found in this solution, but the total primary eclipses provide the necessary constraints for a reliable value (Wilson 1978; Terrell and Wilson 2005). Throughout the solution iteration process, the third-light corrections were negligibly small and often negative.

4.3. Spot model

The light curve asymmetries seen in Figure 9 are usually attributed to magnetic activity that causes cool spots or hot regions (faculae) in the star's photosphere. In Algol systems, a gas stream from the donor star can also form a hot spot on its companion from impact heating. The residuals in Figure 9 show the same asymmetries in all four colors: a small loss of light between orbital phases 0.05 and 0.30 and two small peaks of excess light at phases 0.40 and 0.60. To model these asymmetries, several different spot configurations were modeled using the BM3 program. The spot parameters, latitude, longitude, spot size, and temperature were adjusted until asymmetries were minimized. The process was repeated several times using different numbers of spots (1 to 3) and spot configurations until the asymmetries and residuals were minimized. The best-fit parameter values were then incorporated into a new WD model. The final spotted model resulted in a much-improved fit, with a 57% reduction in residuals compared to the spotless model. This model is not definitive; other spot configurations may give equal or better results. It does indicate that the light curve asymmetries are likely caused by star spots and that the stars are magnetically active. The final spotted solution parameters are shown in column 3 of Table 6. Figure 10 displays the spotted model fit (solid lines) overlaid on the observed light curves. Figure 11 shows a graphical representation of LO UMa created using BM3 (Bradstreet and Steelman 2002).

5. Discussion

The provisional absolute orbital and stellar parameters for each star can be determined with knowledge of one of the star's masses and the mass ratio. There are no spectroscopic observations currently available to directly determine the stellar masses, but the primaries in Algol systems are typically main

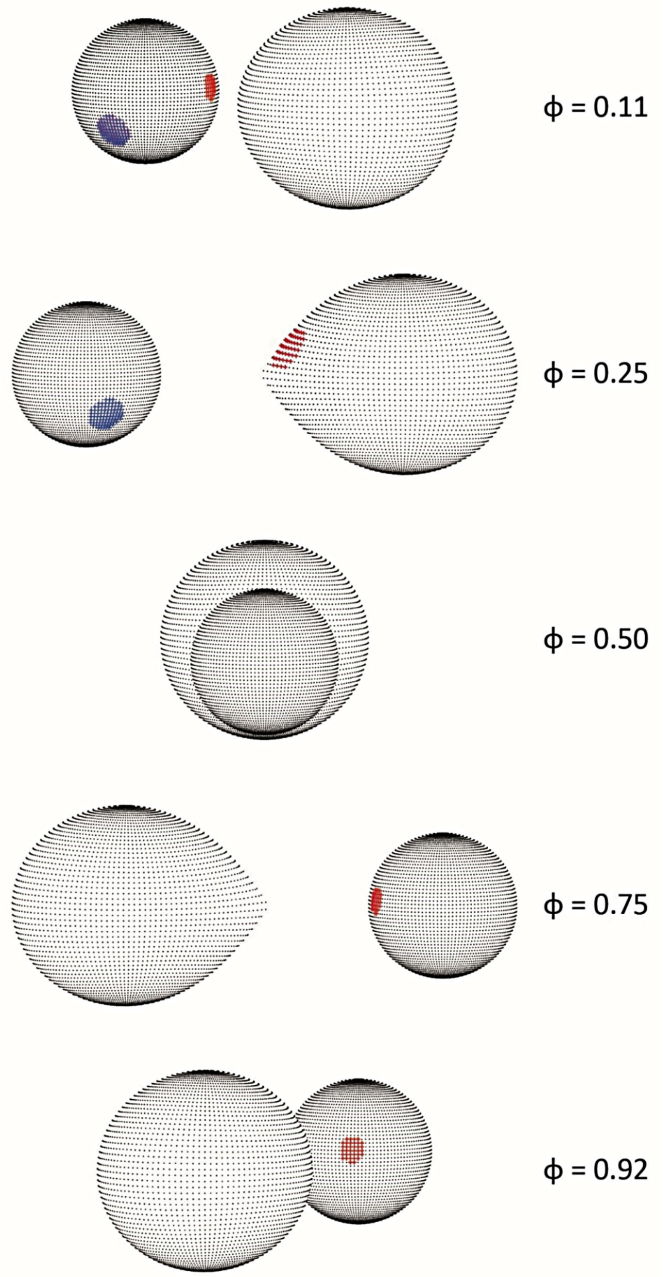

Figure 11. Roche Lobe surfaces of the best–fit WD spot model showing spot locations. The orbital phase is shown next to each diagram.

sequence stars. The mass of those stars can be estimated from their spectral type. The primary's mass, $M_1 = 1.10 \pm 0.11\,M_\odot$, was interpolated from Table 5 of Pecaut and Mamajek (2013) using its effective temperature. This mass, combined with the spotted WD solution mass ratio, gives a secondary mass of $M_2 = 0.68 \pm 0.07\,M_\odot$. Applying Kepler's Third Law gives the distance between the mass centers as $7.7 \pm 0.2\,R_\odot$. The bolometric magnitudes, radii, and surface gravities of the stars were calculated by the WD light curve program (LC). The stellar luminosities, $L_1 = 3.7 \pm 0.4\,L_\odot$ and $L_2 = 1.5 \pm 0.4\,L_\odot$, were computed using the LC bolometric magnitudes in the following equation:

$$M_{bol} = 4.74 - 2.5 \log \left(\frac{L}{L_\odot}\right). \quad (10)$$

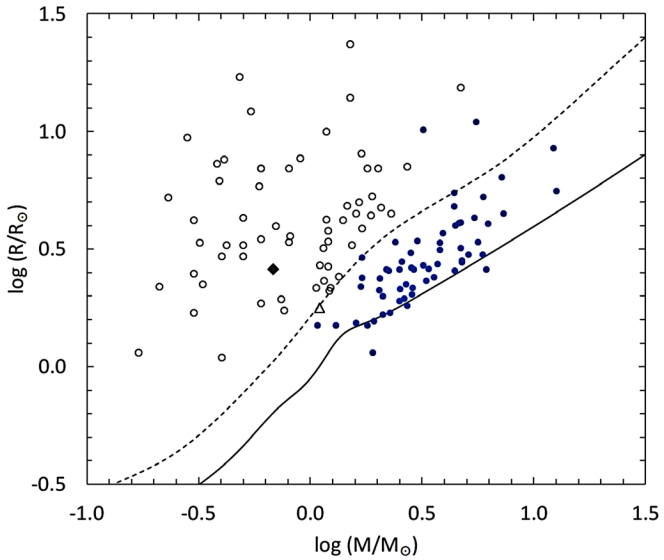

Figure 12. Positions of both components of LO UMa on the Mass-Radius diagram of 62 semidetached Algol systems with well-determined parameters. Closed circles are the primary stars and open circles the secondary stars. The triangle and the diamond are the primary and the secondary of LO UMa, respectively. Solid and dotted lines refer to ZAMS and TAMS, respectively (Tout *et al.* 1996).

The total system luminosity, $L_{12} = 5.2 \pm 0.7\,L_\odot$, is in good agreement with the value calculated in section 4.1 using observed quantities, $5.5 \pm 0.3\,L_\odot$. All the provisional stellar parameter values are collected in Table 7. The distance modulus gives a distance of 853 ± 145 pc, which is consistent with the Gaia distance of 863^{14}_{18} pc (Bailer-Jones *et al.* 2021; Gaia 2016, 2018). In Figure 12, the provisional radii and masses of LO UMa are compared with the values from 62 semi-detached systems with well-determined absolute parameters (Ibanoğlu *et al.* 2006). The zero-age main sequence lines (ZAMS) and the terminal-age main sequence (TAMS) lines are displayed in Figure 12 as well. The primary component of LO UMa (triangle point) has one of the lowest masses of this group and a larger radius compared to a ZAMS star of the same mass. The secondary component (diamond point) is located above the TAMS line indicating an evolved star.

In the period study (see section 2), the parameter values of the three LITE solutions are comparable, but there was one significant difference. The LITE-2 solution gave an orbital eccentricity of $e = 0.42 \pm 0.04$ and a period of $P_3 = 16.4 \pm 0.03$ y for the tertiary component. LITE-3 gave similar values, with $e = 0.47 \pm 0.33$ and $P_3 = 18.6 \pm 0.3$ y. These eccentricity values differ by only 11%, but the error in LITE-3 is very large, as is the error for the time of periastron passage ($T_0 = 2454771 \pm 403$ HJD). The large errors are likely the result of the sparse coverage, large data gaps, and the lower accuracy of the minima timings from the years 1939−1999. The main difference between the LITE solutions concerns the long-term period change given by the quadratic coefficient term (Q). Its value was positive for the LITE-1 solution but negative for LITE-2 and LITE-3. In a close semidetached Algol binary, conservative mass exchange from the less massive Roche-lobe-filling component to the more massive star always causes an increase in orbital period ($Q > 0$). Matter transferred through the inner Lagrangian point

may hit the primary star, causing impact heating, or miss the primary and form a gaseous disk around the star. The distance separating the component stars (A_{orb}) and the radius of the primary determine which one of these configurations occurs. The minimum primary-star radius required for the formation of a gaseous disk was calculated from an empirical relationship derived by Nanouris *et al.* (2015):

$$R_{min} = (0.04930 + 0.03387 \log q + 0.05915 (\log q)^2) A_{orb}, \quad (11)$$

where q is the mass ratio. The resulting value, $R_{min} = 0.345 \pm 0.002\ R_\odot$, is much smaller than the estimated radius for this star ($1.78\ R_\odot$). This means the matter stream would collide with the primary star. The hot spot modeled on the side of the primary star facing the secondary suggests mass transfer is presently active. The downward parabolic O−C diagrams found in the LITE-2 and LITE-3 solutions suggest just the opposite of LITE-1: the orbital period is decreasing ($Q < 0$; see Figures 6 and 7). This implies a nonconservative mass-loss process, which is usually attributed to magnetic braking caused by a coupling between the magnetic field and stellar winds in low-mass stars. The spots found in the light curve solution support current magnetic activity on both stars. This non-conservative mass loss would remove orbital angular momentum from the system, leading to a downward parabolic O−C curve and a long-term decrease in the orbital period. In a comprehensive study on the efficiency of O−C diagrams for diagnosing long-term period changes, it was found that a combination of the mass transfer process and wind-driven mass loss may be at work in close binaries (Nanouris *et al.* 2011, 2015; Erdem and Öztürk 2014). In semidetached systems, these two mechanisms may be strongly competitive. Based on the LITE-2 solution, the period of LO UMa is decreasing at a rate of 4.5×10^{-7} d yr^{-1}, or 4 seconds per century. The LITE-3 solution, with its much longer temporal base (82 years), also supports a decreasing orbital period.

The period modulation found in the O−C residuals was presented as evidence for a third body orbiting the system's barycenter. Cyclical orbital-period variation in binary systems is common; it is observed in 49% of Algols and 64% of W-UMa systems (Liao and Qian 2010). The sinusoidal-like behavior found in the period analysis of LO UMa is mostly supported by CCD minima timings collected over the past 21 years. This time interval is less than two cycles of the proposed orbital period (P_3). This third-body hypothesis should therefore be considered preliminary. Another 10–15 years of precision minimum times will be necessary to confirm that the period modulation is continuing as predicted and thus to prove the existence of the tertiary component. Those future observations could also confirm that the binary's orbital period is decreasing and reduce the errors in the orbital parameters. The LITE solutions indicate the tertiary component has a minimum mass between $1.6\ M_\odot$ and $1.8\ M_\odot$, yet the light curve solutions found no evidence of excess luminosity ($l_3 = 0$). A main sequence star of this mass would have a spectral type of F0, but the LAMOST spectra gives an F9 spectral type that is consistent with the observed color. A massive orbiting object not emitting normal stellar radiation would suggest that it is a noninteracting compact stellar object. With the minimum mass above the Chandrasekhar limit of $\simeq 1.4\ M_\odot$, the tertiary component would most likely be a neutron star. If the orbit has a high inclination i_3, a black hole is also possible. The LITE-2 solution gives periastron distance between this object and the binary of 5.6 ± 0.4 AU ($i_3 = 90°$) and an apastron distance of 13.7 ± 0.4 AU. The barycenter is almost equally distant between the binary and the tertiary object. A compact object of this mass and distance would play a significant role in the evolution of this system.

6. Conclusions

Multiband CCD photometric observations collected in V, g', r', and i' bands resulted in the first precision light curves for LO UMa and two new minimum times for primary eclipse. The light curves displayed deep total primary eclipse and shallow secondary eclipse. Light curve modeling with the WD program found the binary configuration to be semidetached, with primary and secondary stars of spectral types F9 and K8, respectively. Three spots were included in the final Roche model to address light curve asymmetries: a cool spot and a hot spot on the primary star and a single hot spot on the secondary star. This spotting is an indication of magnetically active stars. The linear ephemeris was updated using CCD minima timing observations from the years 1999–2021. A detailed analysis of the O−C diagram found the orbital period of LO UMa is undergoing a sinusoidal variation superimposed on a downward parabolic change. The downward parabolic change indicates that the orbital period of the binary is decreasing due to a combination of magnetic braking and mass transfer. Two possible causes for the period modulation were investigated: the existence of an object of significant mass that is gravitationally bound to the binary and the Applegate effect. The Applegate mechanism requires a certain amount of energy to build a strong magnetic field to drive a dynamo cycle that causes the period variations. Calculations showed the energy available from the secondary star was insufficient to drive the Applegate mechanism. The results of the LITE analysis showed that an object orbiting in either a circular or an elliptical revolution would explain the period modulation. The best-fit LITE solution gave the third body's orbital eccentricity as 0.42 and its minimum mass as $1.6\ M_\odot$. Given this mass, the object is hypothesized to be a neutron star.

LO UMa is an interesting system worthy of additional study. A spectroscopic study would be particularly useful to gain a better understanding of this binary system. Radial velocity measurements are needed to pin down the individual masses and separation distance of the binary stars. Velocity changes in the binary's barycenter could provide supporting evidence for the unseen companion. Spectroscopy could also check the metallicity of the binary stars for possible contamination from a supernova which would have formed the neutron star. Precision CCD minima timings over many years will be very important in confirming the third body and the decreasing orbital period of the binary.

7. Acknowledgements

This research was made possible through use of the AAVSO Photometric All-Sky Survey (APASS), funded by the Robert Martin Ayers Sciences Fund. This research has made use of the SIMBAD database and the VizieR catalog access tool, operated at CDS, Strasbourg, France. This work has made use of data from the European Space Agency (ESA) mission Gaia (https://www.cosmos.esa.int/gaia), processed by the Gaia Data Processing and Analysis Consortium (DPAC, https://www.cosmos.esa.int/web/gaia/dpac/consortium). Funding for DPAC has been provided by national institutions, in particular the institutions participating in the Gaia Multilateral Agreement.

References

Applegate, J. H. 1992, *Astrophys. J.*, **385**, 621.
Bailer-Jones, C. A. L., Rybizki, J., Fouesneau, M., Demleitner, M., and Andrae, R. 2021, *Astron. J.*, **161**, 147.
Baldwin, M. E., Guilbault, P. R., Henden, A. A., Kaiser, D. H., Lubcke, G. C., Samolyk, G., and Williams, D. B. 2001, *J. Amer. Assoc. Var. Star Obs.*, **29**, 89.
Bradstreet, D. H., and Steelman, D. P. 2002, *Bull. Amer. Astron. Soc.*, **34**, 1224.
Butters, O. W., *et al*. 2010, *Astron. Astrophys.*, **520**, L10 (SuperWASP, https://wasp.cerit-sc.cz/form).
Diethelm, R. 2003, *Inf. Bull. Var. Stars*, No. 5438, 1.
Diethelm, R. 2004, *Inf. Bull. Var. Stars*, No. 5543, 1.
Diethelm, R. 2009, *Inf. Bull. Var. Stars*, No. 5894, 1.
Diethelm, R. 2010, *Inf. Bull. Var. Stars*, No. 5945, 1.
Diethelm, R. 2011, *Inf. Bull. Var. Stars*, No. 5992, 1.
Diethelm, R. 2012, *Inf. Bull. Var. Stars*, No. 6029, 1.
Erdem, A., and Öztürk, O. 2014, *Mon. Not. Roy. Astron. Soc.*, **441**, 1166.
Gaia Collaboration, *et al.* 2016, *Astron. Astrophys.*, **595A**, 1.
Gaia Collaboration, *et al.* 2018, *Astron. Astrophys.*, **616A**, 1.
Green, G. M., *et al.* 2018, *Mon. Not. Roy. Astron. Soc.*, **478**, 651.
Henden, A. A., *et al.* 2015, AAVSO Photometric All-Sky Survey, data release 9, (https://www.aavso.org/apass).
Hübscher, J., and Lehmann, P. B. 2015, *Inf. Bull. Var. Stars,* No. 6149, 1.
Hübscher, J., Lehmann, P. B., Monninger, G., Steinbach, H.-M., and Walter, F. 2010, *Inf. Bull. Var. Stars*, No. 5918, 1.
Ibanoğlu, C., Soydugan, F., Soydugan, E., and Dervişoğlu, A. 2006, *Mon. Not. Roy. Astron. Soc.*, **373**, 435.
Irwin, J. 1959, *Astron. J.*, **64**, 149.
Jayasinghe, T., *et al.* 2019, *Mon. Not. Roy. Astron. Soc.*, **486**, 1907.
Kafka, S. 2017, variable star observations from the AAVSO International Database (https://www.aavso.org/aavso-international-database).
Krajci, T. 2005, *Inf. Bull. Var. Stars*, No. 5592, 1.
Kreiner, J. M. 2004, *Acta Astron.*, **54**, 207.
Kurucz, R. L. 2002, *Baltic Astron.*, **11**, 101.
Kwee, K. K., and van Woerden, H. 1956, *Bull. Astron. Inst. Netherlands*, **12**, 327.
Lanza, A. F., and Rodonò, M. 1999, *Astron. Astrophys.*, **349**, 887.
Liao, W.-P., and Qian S.-B. 2010, *Mon. Not. Roy. Astron. Soc.*, **405**, 1930.
Locher, K. 2005, *Open Eur. J. Var. Stars*, **3**, 1.
Locher, K., Blättler, E., and Diethelm, R. 2002, *BBSAG Bull.*, No. 128, 1 (http://www.variables.ch/observations_BBSAG.html).
Lucy, L. B. 1968, *Astrophys. J.*, **151**, 1123.
Luo, A-Li., *et al.* 2015, *Res. Astron. Astrophys.*, **15**, 1095.
Mirametrics. 2015, Image Processing, Visualization, Data Analysis, (https://www.mirametrics.com).
Nagai, K. 2009, *Bull. Var. Star Obs. League Japan*, **48**, 1.
Nanouris, N., Kalimeris, A., Antonopoulou, E., and Rovithis-Livaniou, H. 2011, *Astron. Astrophys.*, **535A**, 126.
Nanouris, N., Kalimeris, A., Antonopoulou, E., and Rovithis-Livaniou, H. 2015, *Astron. Astrophys.*, **575A**, 64.
Paschke, A. and Brat, B. 2021, O–C Gateway (http://var2.astro.cz/ocgate/).
Pecaut, M. J., and Mamajek, E. E. 2013, *Astrophys. J., Suppl. Ser.*, **208**, 9 (http://www.pas.rochester.edu/~emamajek/EEM_dwarf_UBVIJHK_colors_Teff.txt).
Qian, S.-B., Zhang, J., He, J.-J., Zhu, L.-Y., Zhao, E.-G., Shi, X.-D., Zhou, X., and Han, Z.-T. 2018, *Astrophys. J. Suppl. Ser.*, **235**, 5.
Ruciński, S. M. 1969, *Acta Astron.*, **19**, 245.
Shappee, B. J., *et al.* 2014, *Astrophys. J.*, **788**, 48.
Terrell, D., and Wilson, R. E. 2005, *Astrophys. Space Sci.*, **296**, 221.
Tout, C. A., Pols, O. R., Eggleton, P. P., and Han, Z. 1996, *Mon. Not. Roy. Astron. Soc.*, **281**, 257.
van Hamme, W. 1993, *Astron. J.*, **106**, 2096.
van Hamme, W. V., and Wilson, R. E. 1998, *Bull. Amer. Astron. Soc.*, **30**, 1402.
Völschow, M., Schleicher, D. R. G., Perdelwitz, V., and Banerjee, R. 2016, *Astron. Astrophys.*, **587A**, 34.
Williams, D. B. 2001, *Inf. Bull. Var. Stars*, No. 5084, 1.
Wilson, R. E. 1978, *Astrophys. J.*, **224**, 885.
Wilson, R. E., and Devinney, E. J. 1971, *Astrophys. J.*, **166**, 605.
Zasche, P., Liakos, A., Niarchos, P., Wolf, M., Manimanis, V., and Gazeas, K. 2009, *New Astron.*, **14**, 121.